electronics

MDPI

Article

Automatic Classification of Rotating Rectifier Faults in Brushless Synchronous Machines

Kumar Mahtani [1,*], Julien Decroix [2], Rubén Pascual [1], José M. Guerrero [3] and Carlos A. Platero [1]

[1] Department of Electrical Engineering, Escuela Técnica Superior de Ingenieros Industriales, Universidad Politécnica de Madrid, 28006 Madrid, Spain
[2] Interdisciplinary Research Group in Energy Modeling, Paris-Saclay University, 91190 Gif-sur-Yvette, France
[3] Department of Electrical Engineering, Escuela de Ingeniería de Bilbao, Universidad del País Vasco, 48013 Bilbao, Spain
* Correspondence: kumar.mahtani@upm.es

Abstract: This paper presents an advanced automatic fault classification method for detecting rotating rectifier faults in brushless synchronous machines (BSMs). The proposed approach employs a multilayer perceptron (MLP) neural network to classify the operational states of the rotating rectifier, including healthy conditions and common fault types: open-diode (OD), shorted-diode (SD), and open-phase (OP). Key machine measurements, available on an ordinary basis in the industry, such as active power (P), reactive power (Q), stator voltage (U), and excitation current (I_e), are used as inputs for this model, allowing for non-invasive, real-time fault detection. This model achieved an overall classification accuracy of 93.4%, with a precision of 94.9% for fault detection and strong recall performance across multiple fault types. The neural network's robustness is enhanced by advanced data processing techniques, including Gaussian filtering and class balancing through the synthetic minority over-sampling technique (SMOTE). Experimental testing on a modified 5-kVA BSM setup, where rectifier faults were systematically induced, was used to train the network and validate the model's performance. This method provides a promising tool for real-time condition monitoring of BSMs, improving machine reliability and minimizing downtime in industrial applications.

Keywords: brushless machines; classification; condition monitoring; fault detection; fault protection; rectifier; synchronous machines

Citation: Mahtani, K.; Decroix, J.; Pascual, R.; Guerrero, J.M.; Platero, C.A. Automatic Classification of Rotating Rectifier Faults in Brushless Synchronous Machines. *Electronics* **2024**, *13*, 4667. https://doi.org/10.3390/electronics13234667

Academic Editor: Wei Hua

Received: 30 October 2024
Revised: 18 November 2024
Accepted: 25 November 2024
Published: 26 November 2024

1. Introduction

Brushless synchronous machines (BSMs) have become essential in many industrial applications, such as power generation. These machines are widely appreciated for their reliability, ease of maintenance, and robustness, particularly in applications where brushless designs are favored due to their avoidance of brush–slip ring sliding contacts [1,2]. The protection of BSMs is guided by various general [3] and specific [4,5] standards that address the supervision and protection functions typically implemented for excitation systems, such as loss-of-field protection, exciter phase unbalance protection, or several protective functions for specific exciter components [6].

One of the key components of BSMs, the rotating rectifier, remains a source of potential faults that can impact machine performance and lifespan. The rotating rectifier in BSMs is responsible for converting the AC voltage generated by the exciter into DC voltage, which is then supplied to the main machine's field winding [1,7], as illustrated in Figure 1. The rotating rectifier consists of a diode bridge mounted on the rotor, which, due to its rotating nature, is difficult to access and monitor. This limited accessibility, combined with the mechanical and electrical stresses experienced by the rectifier, makes fault detection in rotating rectifiers particularly challenging. Common faults include open-diode (OD), shorted-diode (SD), and open-phase (OP) faults, each of which impacts machine operation in a different manner.

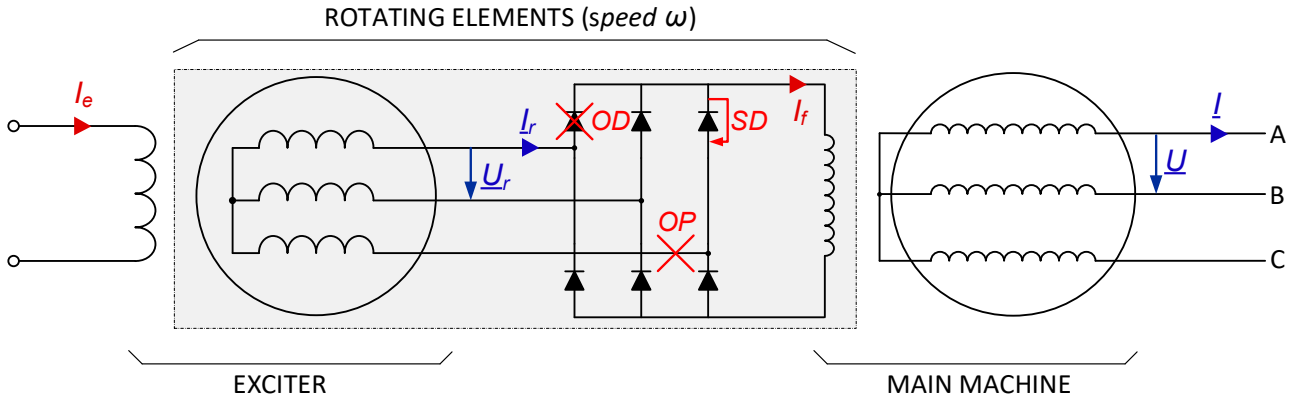

Figure 1. Simplified schema of the BSM [OD: open-diode fault; SD: shorted-diode fault; OP: open-phase fault].

Rotating rectifier faults, if left undetected, can lead to degraded machine performance, reduced efficiency, overheating, and even catastrophic damages and failure of the exciter or main machine components [8]. For instance, open-diode faults degrade the transient response and increase ripple in the output voltage, while shorted-diode faults can cause phase-to-phase armature short-circuits, resulting in severe overloads to the exciter. Open-phase faults, on the other hand, affect the entire branch of the rectifier, leading to a significant reduction in performance. These faults are often fast-developing and can be triggered by grid shocks, mechanical stress, or the aging of semiconductors. The increased rectifier voltage required to compensate for the fault condition is usually supplied by an increased exciter field current [9].

In industrial practice, fuses are employed in each phase of the rotating rectifier to remove any failed diodes from service and, therefore, protect the exciter and the other diodes from overcurrent. In critical applications, such as in nuclear power plants, each phase of the rectifier is usually equipped with two uses connected in parallel to achieve greater system redundancy in case of fuse blow-out due to transitory conditions [10].

Recent research has shown that early detection of such faults [11,12] could improve machine reliability and reduce downtime. Traditional methods of fault detection involve off-line testing, as they rely on manual inspections or off-line diode tests, which require downtime and labor-intensive procedures. Given these limitations, there is a growing need for advanced fault detection systems that can operate online and in real time. In this sense, the most extended online techniques involve the analysis of electrical or mechanical signals. However, most state-of-the-art methods can be invasive and computationally heavy.

This research aims to address these challenges by proposing an automatic fault classifier based on artificial neural networks (ANNs) that can detect and classify faults in rotating rectifiers of BSMs. The ANN approach targets the most common faults in the rotating rectifier of BSMs, such as open-diode, shorted-diode, and open-phase conditions. The proposed method provides real-time fault detection and classification, offering advantages over existing methods in the following practical terms:

- Elimination of the need for specialized diagnostic relays or additional sensors;
- Non-invasive nature, avoiding installation constraints;
- Low computational complexity, enabling efficient real-time diagnostics without spectral analysis;
- Elimination of machine-specific parameter availability requirements;
- Robustness to noise and operational variability.

The present work is structured as follows. Section 2 describes the working principles of the BSM. Section 3 presents the state of the art for rotating rectifier fault detection in BSMs. Section 4 presents the operational principles of the proposed approach. Section 5 develops the application of the proposed method on a specific experimental test rig with enabled access to the rectifier. Section 6 presents the results achieved from this work.

Finally, Section 7 puts forward the conclusions, pointing out the main contributions and opening avenues for future research.

2. Working Principles of the BSM

A BSM, shown in Figure 1, consists of three main parts: the main machine, the exciter, and the rotating bridge rectifier. The exciter's armature, the bridge rectifier, and the main machine field winding rotate on the same shaft. The exciter and the rotating rectifier together form the excitation system, which supplies the necessary direct current (DC) field to the rotor winding of the main machine. In this section, the electromagnetic and mechanical dynamics of the BSM are presented based on intuitive and simplified models.

Furthermore, under the grid-connected mode, the main machine's voltage (U) and frequency (f) are determined by the grid. Active (P) and reactive (Q) powers are controlled. The common shaft's rotational speed (ω) is locked to the grid's frequency (f), and the number of pair-poles (p) of the main machine is calculated according to Equation (1). This speed is known as the synchronism speed (ω_s). The operation of the machine in grid-connected mode is also described in this section.

$$\omega_s = \frac{60 \cdot f}{p} \tag{1}$$

2.1. Main Machine and Exciter Models

Both the main machine and the exciter can be modeled as wound–field synchronous machines, though the difference is that the exciter has a rotating armature and a static field. Synchronous machines generate AC power based on the interaction of the excitation magnetic field, produced by the DC field current, with the armature windings. This AC power is delivered to the grid in the case of the main machine and to the main machine field winding in the case of the exciter.

The flux linkage in each armature winding (λ_a, λ_b, and λ_c) results from the interaction between the excitation magnetic field and the armature currents. This flux linkage in each phase is determined by the self-inductance of each armature winding (L_s), the mutual inductance between armature windings (M_s), and the mutual inductance between the field winding and each armature winding (L_{mf}), as given in Equations (2)–(4) for phases "a", "b", and "c", respectively. The instantaneous values of armature phase currents are denoted i_a, i_b, and i_c, while the DC field current is represented by i_f.

$$\lambda_a = L_s \cdot i_a + M_s \cdot (i_b + i_c) + L_{mf} \cdot i_f \tag{2}$$

$$\lambda_b = L_s \cdot i_b + M_s \cdot (i_a + i_c) + L_{mf} \cdot i_f \tag{3}$$

$$\lambda_c = L_s \cdot i_c + M_s \cdot (i_a + i_b) + L_{mf} \cdot i_f \tag{4}$$

According to Faraday's Law, the voltages induced in each armature winding, V_a, V_b, and V_c, are related to the electromagnetomotive force or e.m.f., given by the time derivatives $d\lambda_a/dt$, $d\lambda_b/dt$ and $d\lambda_c/dt$ for each phase, as shown in Equations (5)–(7). The resistance of each armature winding is denoted as R_s.

$$V_a = R_s \cdot i_a + \frac{d\lambda_a}{dt} \tag{5}$$

$$V_b = R_s \cdot i_b + \frac{d\lambda_b}{dt} \tag{6}$$

$$V_c = R_s \cdot i_c + \frac{d\lambda_c}{dt} \tag{7}$$

The e.m.f.s. terms can be simplified under the assumption of magnetic linearity, which allows for superposition of flux and, therefore, e.m.f. components. This simpli-

fication enables the modeling of the machine, using a simple electrical equivalent with three independent e.m.f. components: excitation; armature reaction; and armature leakage.

For instance, for the main machine, the excitation is represented by an AC voltage source with E_0 magnitude, while the combined effects of armature reaction and leakage are represented by the voltage drop across the synchronous reactance ($X_{s,main}$), considered constant under linear magnetic conditions. The stator resistance ($R_{s,main}$) is also considered in this electrical equivalent. E_0 corresponds to the e.m.f. inducted under no-load conditions, and its magnitude is proportional to the field current value (I_f) and the operating frequency (f). However, the operating frequency is constant in grid-operation mode. Figure 2 shows the simplified per-phase synchronous machine equivalent models particularized for the exciter and the main machine.

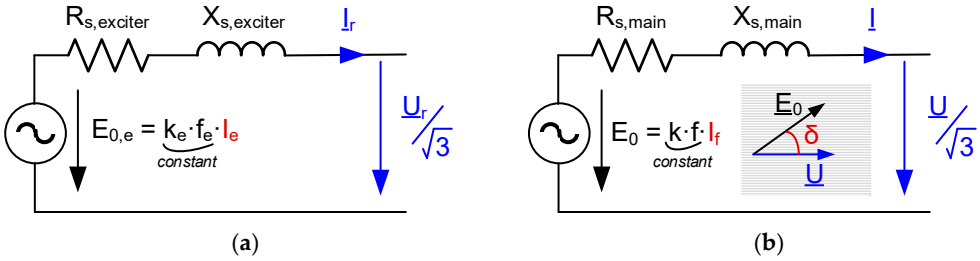

Figure 2. Simplified per-phase equivalent models: (**a**) Exciter; (**b**) Main machine.

In grid-connected mode, the exciter field current I_e is usually regulated by the Automatic Voltage Regulator (AVR) to achieve the desired operating setpoint. The main machine field current I_f is related to I_r in the following.

2.2. Rotating Rectifier Model

The rotating bridge rectifier converts the AC voltage from the exciter's armature into DC voltage to supply the main rotor field. For simplicity, the root mean square (rms) values of the exciter armature phase currents (I_r) and the main field DC current (I_f) are considered. For an ideal three-phase bridge rectifier, Equation (8) is as follows:

$$I_r = I_f \cdot \sqrt{\frac{2}{3}} \tag{8}$$

2.3. Rotational Dynamics

The rotational dynamics, involving torque and speed, are described by Equation (9). This equation expresses the accelerating torque of the common shaft as the difference between the mechanical torque applied by the prime mover (T_m) and the electromagnetic torque produced by the machine (T_e). The mechanical losses, which are proportional to the rotor speed (ω) and the damping coefficient (D), add to the electromagnetic torque. In steady-state conditions, the accelerating torque is zero. The rotor's moment of inertia is denoted by J.

$$J \cdot \frac{d(\omega - \omega_s)}{dt} = J \cdot \frac{d^2\delta}{dt^2} = T_m - T_e - D \cdot \omega \tag{9}$$

The load angle δ is defined, as shown in Figure 2b, as the phase difference between the excitation e.m.f. (the phase of vector $\underline{E}_0$), which aligns with the rotor's position, and the grid voltage ($\underline{U}$), which aligns with the airgap magnetic field rotating at the synchronous speed (ω_s). According to Equation (9), variations in T_m result in changes in δ, which are used for active power control.

2.4. Active and Reactive Power Controls

Since the BSM operates in grid-connected mode, its frequency and voltage are dictated by the grid. Active (P) and reactive (Q) power output controls are performed. The

expressions for P and Q are shown in Equations (10) and (11), respectively. Active power control is achieved by adjusting T_m and, thereby, δ through the turbine governor. Reactive power management is achieved by controlling the exciter field current I_e through the AVR, which has a final effect on I_f and E_0 following the simplified models described throughout this section. A broader context overview of the BSM operating in grid-connected mode as a generator is depicted in Figure 3.

$$P = 3 \cdot \frac{E_0 \cdot \frac{U}{\sqrt{3}}}{X_{s,main}} \cdot sin\delta \tag{10}$$

$$Q = 3 \cdot \frac{E_0 \cdot \frac{U}{\sqrt{3}}}{X_{s,main}} \cdot \left(cos\delta - \frac{U}{\sqrt{3}} \right) \tag{11}$$

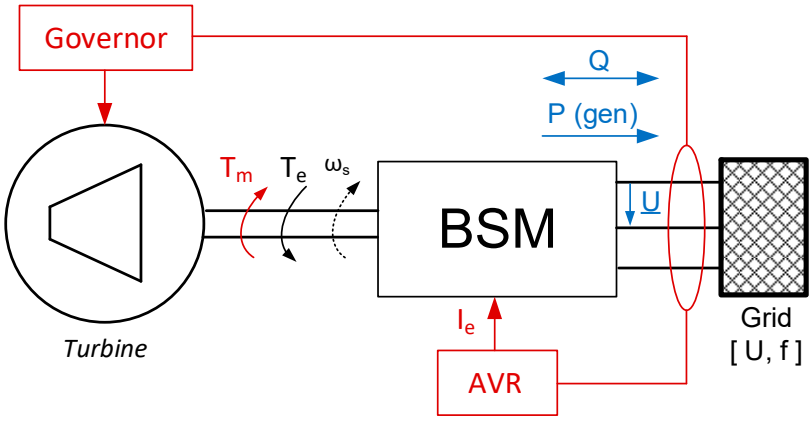

Figure 3. Broader context of the BSM operating under grid-connected mode as a generator.

3. State of the Art

The detection of rotating rectifier faults in BSMs has a long history in the industry, primarily centered around off-line and manual testing methods, which are still being developed in the literature [11,13]. On the other hand, the online detection of these faults has also been widely explored in the literature through several techniques. These methods can be categorized into electrical signal analysis, mechanical signal analysis, thermal imaging, flux analysis, and model-based approaches. Each of these techniques provides unique advantages and challenges when applied to diagnosing rectifier faults such as open-diode, shorted-diode, and open-phase failures. In the following, the most relevant references will be addressed.

3.1. Electrical Signal Signature Analysis

Electrical signal analysis remains one of the most conventional approaches to detecting faults in rotating rectifiers. These methods typically involve monitoring terminal voltage or current, or exciter field current, to identify deviations from normal operation according to known patterns, referred to as signatures.

Voltage-based analysis is widely used to detect faults, especially those affecting the harmonics in the output waveform. It is demonstrated [14,15] that open-diode and shorted-diode faults produce specific changes in the harmonic content of the generator's output voltage. These harmonics are usually detected through techniques such as the Fast Fourier Transform (FFT) or the wavelet transform (WT), which have been successfully applied to detect and classify different types of rotating rectifier faults. However, such methods often suffer from noise susceptibility and can result in false positives (false fault detections) in electromagnetically noisy industrial environments.

Current-based approaches are also prominent. Current monitoring can detect rectifier faults by identifying the imbalances and disturbances from the exciter's armature current

waveform reconstruction [16,17]. The detection process relies on recognizing unbalanced current waveforms, which indicate whether a diode is opened or shorted. The calculation of the exciter rotor armature current is a key factor for the application of these methods [18]. Current-based methods can be susceptible to external noise, require further optimization to handle noisy operating environments, and usually imply a computational burden.

The exciter field current also provides an effective way to detect rotating rectifier faults [17–25]. A key advantage of these methods is that they can monitor the health of the system in real time without invasive measures and with low affection for noise. The harmonic components of the exciter current, particularly the ratio of specific harmonics, such as the second harmonic to the fundamental, have been employed to effectively pinpoint diode faults. Though effective, this technique requires substantial signal processing and harmonic decomposition and can struggle with the computational load in dynamic operating conditions.

Exciter field current monitoring is the most widespread solution in the industry for rotating diode fault diagnostics in BSMs. The ratio between the peak value of the AC ripple superimposed on the exciter field current, and this current itself is monitored. Typically, the input signal is detected as a voltage drop across a resistor placed in series with the exciter field winding. However, this method depends on relay tailoring at procurement. The installation process adds complexity and may require modifications to the machine or its control system, which can be invasive and costly, especially in existing installations.

3.2. Mechanical Signal Analysis

Vibration and acoustic signal analysis provide non-electrical alternatives for fault detection in BSMs. Vibration analysis leverages the mechanical disturbances caused by rectifier faults, which manifest as irregularities in vibration signatures. In [26], the vibration-based methods were applied for fault detection in the rotating rectifier using wavelet transform techniques to classify the vibration signals. These signals were then analyzed using machine learning algorithms like support vector machines (SVMs), which can distinguish between normal and faulty states. This method requires additional sensors that add up to the system cost and may face difficulties, differentiating between electrical and mechanical faults in the machine.

Acoustic analysis, another mechanical method, involves capturing sound waves generated by the machine during operation. This technique is advantageous because it provides an early indication of faults and can be deployed without invasive equipment. In [27], an acoustic-based fault detection system was developed, which used wavelet decomposition and machine learning classifiers to detect faults in BSMs. Nevertheless, the use of acoustic signals is constrained by the need for a quiet operating environment, as its effectiveness decreases in the presence of significant ambient noise.

3.3. Thermal Imaging

Thermal imaging has gained attention as a non-invasive method for detecting faults in electrical machines. This method captures the heat distribution on the surface of the machine, where irregularities indicate potential electrical or mechanical issues. In [28], a novel fault diagnosis approach was proposed using thermography-based analysis in BSMs. In this method, features were extracted from thermal images using wavelet transform techniques, and classifiers like k-nearest neighbors (KNN) were applied to differentiate between healthy states and various faults. This method boasts high classification accuracy, up to 95%, for detecting open-circuit diode faults under different load conditions.

Despite its benefits, thermal imaging requires high-resolution cameras and advanced signal processing to effectively identify subtle temperature differences associated with early-stage faults. Furthermore, thermal changes may take time to manifest, leading to delays in fault detection. The cost and computational complexity involved in processing thermal data can also be a limitation for real-time industrial applications.

3.4. Flux Analysis

Stray and airgap flux monitoring is another powerful diagnostic technique used in BSMs. Stray flux analysis detects the electromagnetic fields generated by faults in the rectifier, making it a non-invasive method that does not require direct access to the rectifier components. In [29], this method was applied to detect diode failures in synchronous generators by analyzing the radial and axial stray flux. The induced electromotive force (EMF) generated in a search coil was analyzed using spectral techniques, allowing for the detection of open-diode faults. In [30], the ability to distinguish between cases of open-diode and shorted-diode has been limited to the no-load conditions and certain loads of specific natures. Stray flux monitoring techniques require the installation of search coils and are characterized by their low accuracy and computational burden.

On the other hand, airgap flux monitoring [31,32], though highly accurate, is invasive as it requires the installation of sensors inside the machine. This method can provide high-resolution fault detection by monitoring the magnetic flux in the air gap between the rotor and stator. However, its drawbacks include installation difficulties and high computational costs.

3.5. Model-Based Methods

Model-based methods involve constructing detailed mathematical models of the machine's normal operation [33–35] and comparing real-time data to theoretical healthy conditions. This approach is often used to identify deviations indicative of faults. Other references leverage finite element analysis (FEA) software as a robust tool to detect rotating rectifier faults under various operating conditions [36]. Notable recent developments have used model-based condition monitoring methods based on theoretical standard methods to predict the actual exciter field current under healthy conditions from the machine output values [8]. By comparing the actual exciter field current with the predicted value, rotating rectifier faults can be detected.

The main advantage of model-based methods is that they provide high precision by simulating specific failure conditions. However, they require detailed knowledge of machine parameters to develop the theoretical models, which may not always be available from the manufacturer or easily obtainable through testing during commissioning or overhauls. This limitation can restrict their applicability in industrial environments.

4. Description of the Proposed Classification Method

The technical challenge addressed by the method proposed in this work is to distinguish the operating state of the rotating rectifier of BSMs, differentiate between healthy and faulty conditions, and classify the type of fault in the latter case. This classification is based exclusively on input features measured from the static components of the system. Specifically, these features include the active power (P), reactive power (Q), and stator voltage (U), in addition to the excitation current (I_e). This selection of inputs corresponds to the variables that are monitored on an ordinary basis in mainstream industrial applications. The machine's condition is classified into four categories: healthy state (H) and three faulty states corresponding to open-diode (OD), shorted-diode (SD), and open-phase (OP). A general representation of the proposed method is presented in Figure 4.

The proposed technique applies machine learning approaches, specifically a multilayer perceptron (MLP) neural network, to classify the operational states of the rotating rectifier in BSMs. This choice is justified by the perceptron's ability to model complex, non-linear relationships between the input features and the output labels in multiclass classification problems. The overall approach is summarized below with a more in-depth explanation of each of the steps.

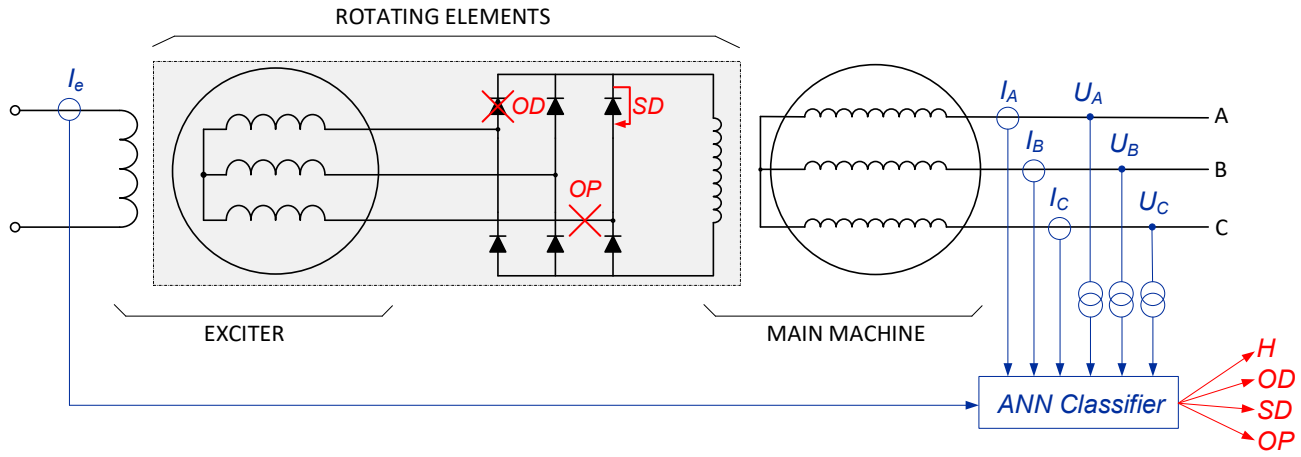

Figure 4. Simplified representation of the proposed classification method.

4.1. Problem Definition

The classification task is framed as a supervised learning problem. Given the input vector $\underline{x}$ = [P, Q, U, I_e] that describes the machine operating point as per Section 2, the goal is to map the machine's operating measurements to a discrete categorical output, indicating the machine's operational condition. Mathematically, this can be described as a multiclass classification problem where this model learns a function f: $R^4 \rightarrow$ {H, OD, SD, OP}. The neural network learns to minimize the discrepancy between its predicted output and the actual state by employing the optimization problem expressed in Equation (12):

$$min_{\underline{\theta}} \sum_{i=1}^{N} L\left(f_{\underline{\theta}}\left(\underline{x_i}\right), y_i\right) \tag{12}$$

In Equation (12), N represents the number of training samples; L designates the loss function; $f_{\underline{\theta}}$ corresponds to the neural network model parametrized by vector $\underline{\theta}$; $\underline{x_i}$ is the input vector of the i-th sample, and y_i is the true label for the corresponding input.

4.2. Neural Network Architecture

The generalized form of the proposed network architecture is illustrated in Figure 5.

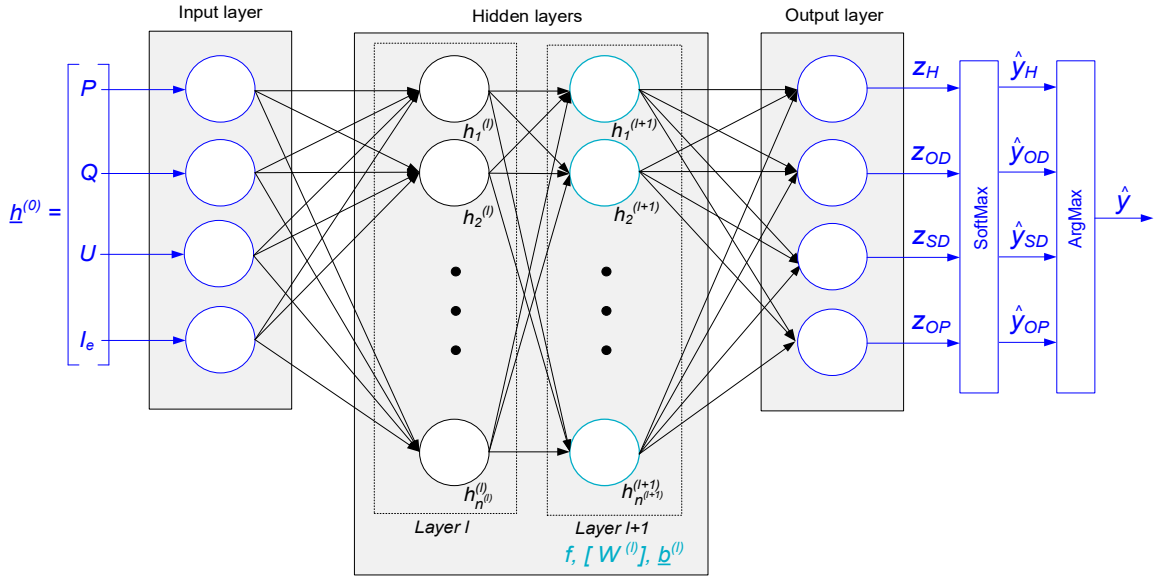

Figure 5. Generalized form of the proposed ANN architecture.

The architecture of the input layer consists of four neurons, each corresponding to the four machine input measurements: P; Q; U; and I_e. This layer simply passes the input vector through to the subsequent layers. The dimensionality of the input space, therefore, is R^4. Mathematically, the input vector at layer $l = 0$ is denoted as per Equation (13):

$$\underline{h}^{(0)} = [P,\ Q,\ U,\ I_e]^T \tag{13}$$

The architecture includes one or more fully connected hidden layers, each with neurons that apply a non-linear transformation to the input data. Each neuron in a given layer is connected to all neurons in the preceding layer. Non-linearity is introduced via an activation function, which ensures that the network can capture intricate patterns within the data. For each hidden layer, the forward pass can be written as per Equation (14):

$$\underline{h}^{(l+1)} = f\left(\left[W^{(l)}\right]\cdot\underline{h}^{(l)} + \underline{b}^{(l)}\right) \tag{14}$$

In Equation (14), $\underline{h}^{(l)}$ and $\underline{h}^{(l+1)}$ correspond to the vector of activations from layer l and $l + 1$, with dimensionalities $n^{(l)}$ and $n^{(l+1)}$, respectively. $[W^{(l)}]$ is the weight matrix for layer l with $[W^{(l)}] \in R[n^{(l)} \times n^{(l+1)}]$; $\underline{b}^{(l)}$ represents the bias vector for layer l with $\underline{b}^{(l)} \in R[n^{(l+1)}]$, and f represents the activation function applied element-wise. The number of neurons and layers is tuned based on validation performance, ensuring a balance between underfitting and overfitting, as described later. This tuning process is further discussed in the regularization section.

The output layer has four neurons, one for each class {H, OD, SD, OP}. Each neuron in the output layer represents a logit z_i, which is a raw score indicating the network's confidence in assigning the input to a particular class i. The SoftMax function is applied to the outputs of this layer to convert them into probabilities, i.e., to transform the raw network outputs (logits) into a valid probability distribution over the classes. The SoftMax function for class i is defined following Equations (15) and (16):

$$\hat{y}_i = \frac{\exp(z_i)}{\sum_{j=1}^{C}\exp(z_j)} \tag{15}$$

$$\sum_{i=1}^{C}\hat{y}_i = 1 \tag{16}$$

In Equations (15) and (16), z_i is the raw output (logit) for class i, and $\hat{y}_i$ represents the predicted probability that the input belongs to class i, while C is the number of classes (C = 4 in this case). The SoftMax function ensures that the output values are normalized into non-negative values that sum to 1, making them interpretable as probabilities, which are used in the loss function to evaluate the accuracy of matching the true labels. The network's final predicted class is the one with the highest probability, given by Equation (17). This final step yields the network's predicted label for the input, based on which output neuron has the highest activation.

$$\hat{y} = argmax_i[\hat{y}_i] \tag{17}$$

4.3. Training Process

The training process of the neural network involves optimizing the model's parameters by minimizing the loss function. The categorical cross-entropy loss function is used to measure the error between the predicted probability distribution $\hat{y}$ and the true distribution y, expressed as a one-hot encoded vector. This function measures the divergence between the predicted probability distribution and the true label distribution, allowing this model

to adjust its internal parameters (weights and biases) to improve classification accuracy. The expression of the loss function is given by Equation (18):

$$L\left(\underline{p}, \underline{q}\right) = -\sum_{i=1}^{C} p_i \cdot log(q_i) \tag{18}$$

In Equation (18), p_i is the true label probability distribution (1 for the correct class, 0 for the others); q_i is the predicted probability distribution output by the SoftMax function. This loss function calculates the negative log-likelihood for the true class. For the entire dataset with N samples, the total loss L_{total} is the sum of the losses across all samples, as expressed in Equation (19):

$$L_{total} = \sum_{i=1}^{N} \left[-\sum_{i=1}^{C} p_i \cdot log(q_i) \right] \tag{19}$$

The gradient of the loss function with respect to the weights is computed using backpropagation, which allows us to iteratively update the model's parameters (weights and biases) to minimize L_{total}, thus guiding the network toward better performance on the classification task. The minimization of the loss through the gradient descent technique with backpropagation adopts the following mathematical form for the update of specific weights $w_{i,j}$ connecting neuron i to neuron j, from iteration t to iteration (t + 1):

$$w_{i,j}^{(t+1)} = w_{i,j}^{(t)} - \eta \cdot \frac{\partial L}{\partial w_{i,j}} \tag{20}$$

In Equation (20), η represents the learning rate, a hyperparameter that controls the step size in the weight updates, and the partial derivative designates the gradient of the loss function with respect to the corresponding weight $w_{i,j}$. The backpropagation algorithm efficiently computes these gradients by applying the chain rule to propagate errors backward through the network, from the output layer to the input layer, as expressed in Equation (21), using the pre-activation value z_j for neuron j, defined as the weighted sum of the inputs to neuron j as per Equation (22). The partial derivative of the pre-activation value with respect to the weight corresponds to no other than the activation of neuron i from the previous layer.

$$\frac{\partial L}{\partial w_{i,j}} = \frac{\partial L}{\partial z_j} \cdot \frac{\partial z_j}{\partial w_{i,j}} \tag{21}$$

$$z_j = \sum_i \left(w_{i,j} \cdot h_i + b_j \right) \tag{22}$$

Specifically, the backpropagation algorithm calculates the error term for each neuron j in the network, denoted as δ_j, starting from the output layer and propagating back to the input layer. The error term for output layer neurons is computed as the difference between the predicted probability and the true label for class j (1 if the sample belongs to class j, 0 otherwise), as per Equation (23). For hidden layer neurons, the error term is computed using the error terms of the subsequent layer, as given in Equation (24), with f' corresponding to the derivative of the activation function applied to neuron j.

$$\delta_j = \hat{y}_j - y_j \tag{23}$$

$$\delta_j = \left(\sum_k w_{j,k} \cdot \delta_k \right) \cdot f'(z_j) \tag{24}$$

The general representation of the training process is provided in Figure 6.

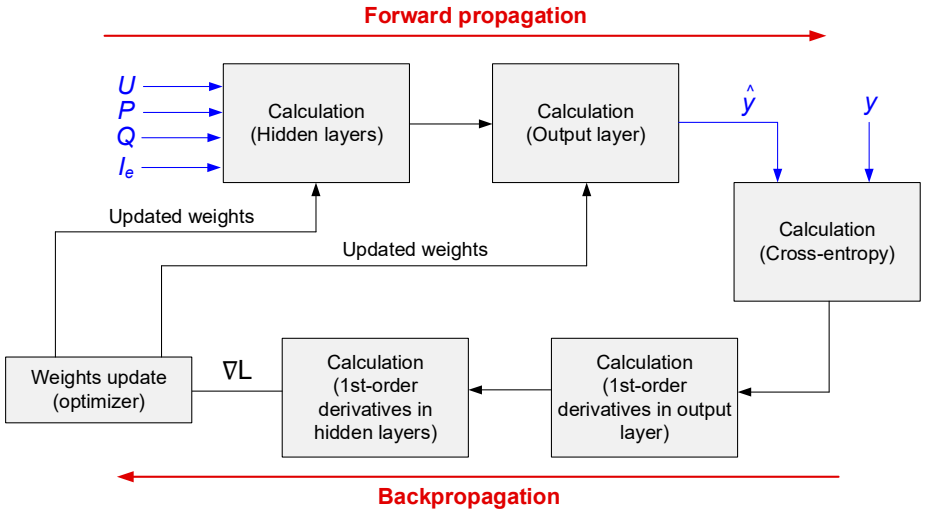

Figure 6. Simplified representation of the training process.

In the actual training, data are processed in mini-batches to improve computational efficiency. Instead of updating the weights after each individual training sample (as in stochastic gradient descent) or after the entire dataset (as in batch gradient descent), mini-batch gradient descent updates the weights after processing small batches of samples. Therefore, Equation (20) can be rewritten into Equation (25), assuming that each mini-batch is size B, and that the gradients are averaged across the mini-batch samples.

$$w_{i,j}^{(t+1)} = w_{i,j}^{(t)} - \eta \cdot \frac{1}{B} \cdot \sum_{b=1}^{B} \frac{\partial L}{\partial w_{i,j}^{(b)}} \tag{25}$$

The entire dataset is passed through the network multiple times during training, known as epochs. For each epoch, the weights are updated iteratively for each batch, and the network adjusts based on the cumulative errors across the dataset. The number of epochs and batch size are hyperparameters to be carefully chosen to optimize performance. A higher number of epochs allows the network to learn more, but an excessive number of epochs may lead to overfitting. Similarly, smaller batch sizes lead to more frequent updates, but they may introduce more noise in the gradient estimates.

4.4. Regularization and Generalization

In the context of machine learning, regularization is essential to prevent this model from overfitting the training data. Overfitting occurs when this model becomes overly complex, fitting the noise and peculiarities in the training data rather than general patterns that are useful for new, unseen data. Regularization techniques help this model generalize better to new data by adding a penalty to the loss function that discourages overly complex models. Both L1 and L2 regularization have been applied. These techniques introduce penalties in the model's weight magnitudes to control complexities, effectively reducing the model's capacity to rely too much on certain features, thus preventing overfitting.

L1 regularization (Lasso regularization) adds a penalty equal to the absolute value of the magnitude of the weights. L1 regularization tends to sparsify the weight vector, driving some weights corresponding to unimportant features to zero, making it useful for feature selection. On the other hand, L2 regularization (Ridge regularization), also known as weight decay, penalizes the squared magnitude of the weights. L2 regularization discourages large weight values by adding the quadratic penalty, ensuring that all features contribute to this model but with smaller weight magnitudes. Unlike L1, L2 regularization does not drive weights to zero but rather encourages small non-zero values. The sparsity properties of L1 and the smoothness and stability of L2 have been combined in a technique

known as Elastic Net regularization. The adopted combined loss function is expressed in Equation (26):

$$L_{ElasticNet} = L + \alpha_1 \cdot \sum_{i=1}^{n} |w_i| + \alpha_2 \cdot \sum_{i=1}^{n} (w_i)^2 \quad (26)$$

In Equation (26), $L_{ElasticNet}$ represents the final loss function after L1 and L2 regularizations; L represents the original loss function (in this case, the categorical cross-entropy for classification tasks); w_i represents the weights of the mode, and α_1 and α_2 correspond to the regularization parameters that control the strength of L1 and L2 regularizations, respectively.

In addition to regularization, cross-validation is used to further improve the model's ability to generalize unseen data. The method used is k-fold cross-validation, which divides the training data into k subsets, trains this model on (k-1) subsets, and validates it on the remaining subset. This process is repeated k times, each time using a different subset for validation, and the average performance across all folds is taken as the final evaluation metric. Mathematically, in k-fold cross-validation, the model's parameters $\underline{\theta}$ are optimized by minimizing the cross-validation loss, as per Equation (27):

$$\hat{\underline{\theta}} = argmin_{\underline{\theta}} \frac{1}{k} \cdot \sum_{i=1}^{k} L\left(f_{\underline{\theta}}(\underline{x_i}), y_i\right) \quad (27)$$

In Equation (27), $\underline{x_i}$ and y_i are the training and validation sets for fold i, and L designates the loss function, including regularization penalties. Cross-validation helps in choosing hyperparameters such as the regularization strengths α_1 and α_2, as well as other network hyperparameters like the number of layers and neurons.

Another form of regularization that was applied was early stopping. During training, this model may start to overfit the training data after a certain number of epochs. Early stopping monitors the model's performance on a validation set and halts the training process when the validation performance stops improving. This prevents this model from overfitting by reducing the risk of memorizing the training data.

Finally, dropout was also applied as a regularization technique to prevent overfitting by randomly ignoring a fraction of the neurons only during the training process. By doing this, the network learns more robust and generalized representations, as it is forced to rely on different combinations of neurons during each training iteration. For the activations of a given l, with n neurons, layer before dropout $\underline{h}^{(l)} = [h_1, h_2, \ldots, h_n]^{(l)}$, the mask vector $\underline{m}^{(l)}$ is applied to the activations following Equation (28) through the element-wise multiplication the activation vector with the mask vector (Hadamard product). Each element $m_i^{(l)}$ of the mask is a Bernoulli random variable that takes the value 1 with probability p, and 0 otherwise, as per Equation (29).

$$\underset{\sim}{\underline{h}}^{(l)} = \underline{m}^{(l)} \odot \underline{h}^{(l)} \quad (28)$$

$$m_i^{(l)} \sim Bernoulli(p) \quad (29)$$

In Equations (28) and (29), $m_i^{(l)}$ is the binary dropout mask for neuron i; $\underline{m}^{(l)}$ is the mask vector; $\underline{h}^{(l)}$ is the activations vector before dropout, and $\underset{\sim}{\underline{h}}^{(l)}$ corresponds to the dropped activations vector.

4.5. Classification and Interpretation

The neural network learns to distinguish between different operational states by learning decision boundaries in the input space defined by the machine's operating variables (P, Q, U, I_e). This results in a discrete prediction $\hat{y} \in$ {H, OD, SD, OP}. Each fault type corresponds to specific patterns in the machine's operating characteristics [8], and the network adjusts its parameters during training to establish these boundaries. Each state is analyzed in the following:

1. Healthy state (H): When the machine is operating normally, the input variables exhibit stable and expected values based on the machine's specifications. The neural network learns to map this region of the feature space to the healthy class;
2. Open-diode fault (OD): This fault is characterized by a reduction in the rectified voltage and changes in the harmonic content due to a failed diode in the rectifier. This can lead to specific variations in the excitation current (I_e) imposed by the AVR to maintain the machine output setpoint defined by the active and reactive power setpoints [P, Q] or to a drop of reactive power value (Q) if no action is taken in the excitation control. The network identifies this fault based on shifts in these variables, adjusting the decision boundary accordingly;
3. Shorted-diode fault (SD): In the case of a shorted-diode, the machine experiences a more significant voltage drop across the rectifier compared to the open-diode case, as well as distinct harmonic distortions. As presented in the previous case, the excitation current (I_e) tends to increase with AVR in operation, and Q tends to drop in other cases. The network learns to associate these larger shifts with the shorted diode class;
4. Open-phase fault (OP): An open phase results in a phase imbalance in the machine, leading to substantial changes in both the excitation current and power characteristics. Similarly, the network learns the feature that corresponds to the overexcitation imposed by the AVR to compensate for improper asymmetrical rectification conditions or the drop in Q in other cases by learning the unique feature pattern associated with this type of imbalance. The feature is characterized by greater shifts in these variables than OD faults, but it is lower than in SD faults.

5. Experimental Application of the Proposed Classification Method

5.1. Experimental Setup

The first step in applying the methodology described in the previous section is to obtain experimental data from a BSM under various states, including H, OD, SD, and OP. To achieve this, extensive experimental tests were performed at different operational conditions [P, Q, U] on a 5-kVA, 4-pole, 400-V salient-pole BSM. This BSM was modified by incorporating five slip rings and brushes—three on the exciter armature side and two on the main machine field winding side—in order to make the rectifier stationary, thereby allowing access for fault implementation. On the main machine armature, stator voltage (U), active power (P), and reactive power (Q) measurements were acquired via commercial three-channel programmable transducers (0.2 accuracy class for voltage and current measurements; 0.5 accuracy class for other measurements; RS232 computer interface). Additionally, the exciter field current (I_e) was measured using a Hall effect sensor (1% precision amplifier; I2C interface). All data were recorded on a computer using a microcontroller, manufactured by Arduino ®, Monza, Italy. A simplified diagram of the experimental setup is shown in Figure 7.

Furthermore, the actual view of this experimental setup can be observed in Figure 8. The main machine (1) and the exciter (2) are housed within a shared frame. In this setup, the rotating diode rectifier (3), which is normally located on the rotor, is positioned outside the machine. Such a special arrangement was carried out by adding five slip rings and brushes (4) that were incorporated into the exciter's armature winding and the main machine's field winding.

The modified BSM shares its rotating shaft with an induction motor (IM) (5), which is powered through a variable frequency controller (VFC). The excitation power is supplied to the exciter by a variable DC source. The BSM is connected to the grid via an autotransformer and a synchronization cabinet. As the experiments are carried out under grid operation mode, constant frequency or speed, as well as constant output voltage, are ensured. The regulations of P and Q are performed through the variable frequency drive (VFC and IM) and the excitation supply, respectively. Particularly, the drive serves to control P by providing the necessary torque to the shaft, emulating the operation of the turbine's governing system in a power plant.

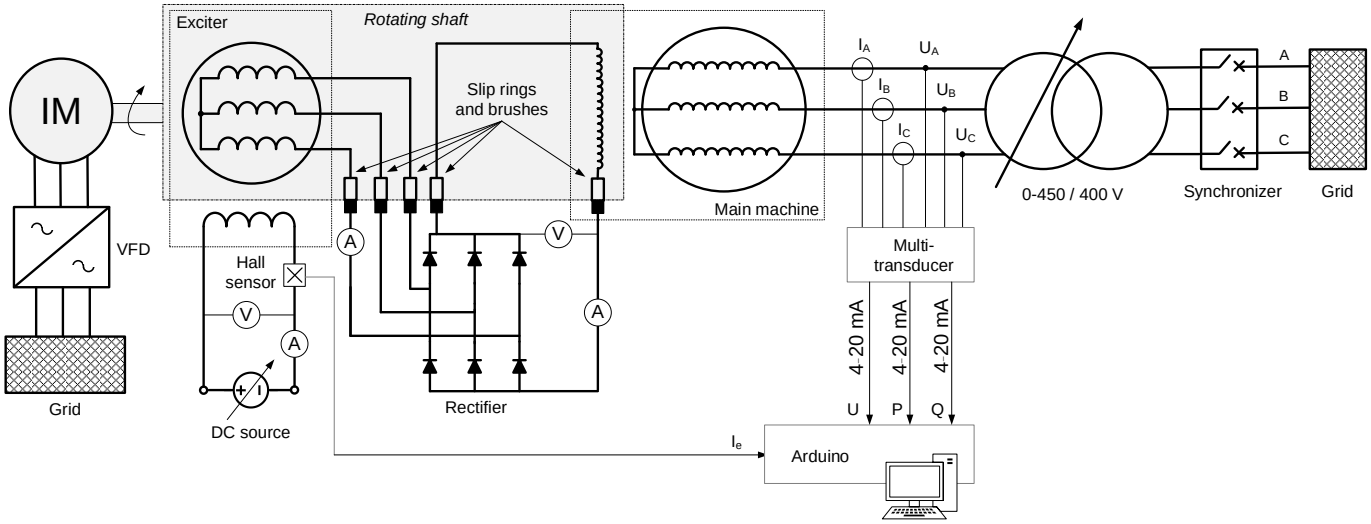

Figure 7. Simplified diagram of the experimental setup.

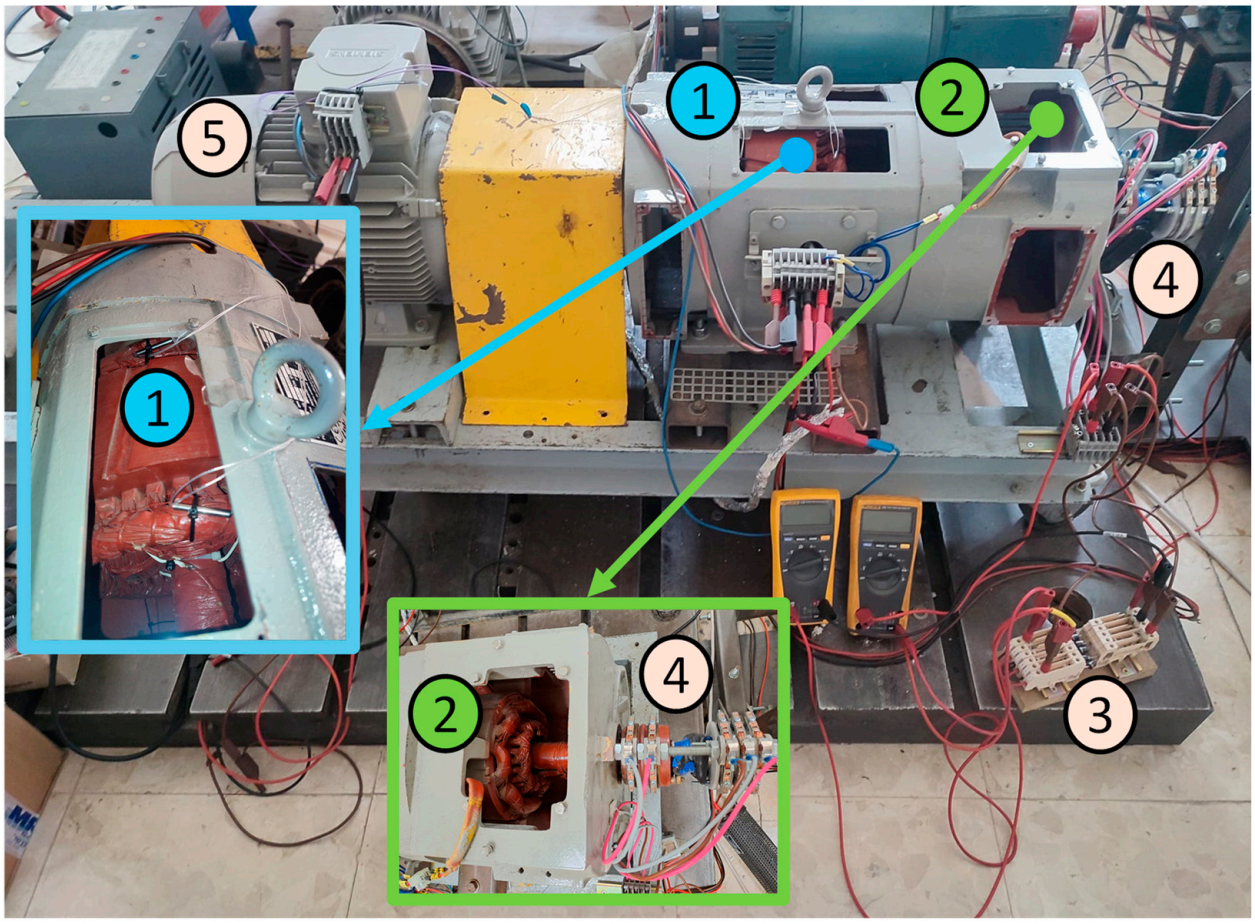

Figure 8. Experimental setup: (1) Main machine; (2) Exciter; (3) Static rectifier; (4) Slip rings and brushes; (5) Induction motor (drive).

The rated nameplate values of both machines—main machine and exciter—included in the experimental BSM system are detailed in Tables 1 and 2, respectively.

Table 1. Main machine-rated values.

Alternator Type	**Synchronous 3-Phase**	
Rated power	5	kVA
Rated speed	1500	rpm
Rated voltage	400	V
Rated current	7.2	A
Pole pairs	2	
Rated frequency	50	Hz
Ingress protection rating (IP)	21	
Insulation class	F	
Rated excitation voltage	33	V
Rated excitation current	4.1	A

Table 2. Exciter-rated values.

Alternator Type	**Synchronous 3-Phase**	
Rated power	277	VA
Rated speed	1500	rpm
Rated voltage	40	V
Rated current	4	A
Pole pairs	4	
Rated frequency	100	Hz
Ingress protection rating (IP)	21	
Insulation class	F	
Rated excitation voltage	33	V
Rated excitation current	0.61	A

5.2. Experimental Data Acquisition and Processing

Each input variable was measured under controlled conditions, where the machine was subjected to different states (H, OD, SD, and OP). The measurements were taken using a combination of high-precision power meters, voltmeters, and current sensors, ensuring accurate and reliable data collection: $\underline{x}_i = [P_i, Q_i, U_i, I_{e,i}]$ for samples *i* to N. The test covered a wide range of operational scenarios, ensuring variability in the input data crucial for training robust machine learning models. The dataset D is constructed as a collection of N samples (N = 12,597,715), each consisting of a feature vector $\underline{x}_i$ and a corresponding label y_i, which denotes the machine's operational state, as expressed in Equations (30) and (31):

$$D = \{(\underline{x}_i,\ y_i) \mid i = 1,\ 2,\ \ldots, N\} \tag{30}$$

$$y_i \in \{H,\ OD,\ SD,\ OP\} \tag{31}$$

Each sample ($\underline{x}_i$, y_i) in the dataset was labeled based on the machine's operating condition during data acquisition. The label y_i is a categorical variable that indicates whether the machine was operating normally (H) or under one of the fault conditions (OD, SD, or OP). The faults were systematically induced during the experimental tests by creating an open or short-circuit in the rectifier or disconnecting a phase of the exciter armature. The recorded electrical variables (P, Q, U, and I_e) exhibited distinct patterns depending on the state, which guided the labeling process.

To improve data quality for fault classification, noise was filtered out from the raw measurements. Several filtering techniques were explored, and the Gaussian filter was selected based on its effectiveness in preserving signal integrity while reducing noise. The Gaussian filter applies a weighted moving average to the signal, where the weights follow a Gaussian distribution. This ensures that data points closer to the target point have a

higher influence on the filtered value. This filtering technique is described by Equation (32) for the filtered signal at index i:

$$y[i] = \sum_{j=-k}^{k} x[i+j] \cdot \frac{1}{\sqrt{2 \cdot \pi \cdot \sigma^2}} \cdot e^{-\frac{j^2}{2 \cdot \sigma^2}} \quad (32)$$

In Equation (32), x[i + j] is the original unfiltered signal at index i + j; σ is the standard deviation of the Gaussian distribution, which controls the width of the filter window, and k is the size of the window, typically chosen as 3σ. The filter smooths the signal, removing high-frequency components. The choice of k is critical, as a small value would not sufficiently reduce noise, while a large value could overly smooth the signal, distorting the machine's operational characteristics. In this case, k = 40 σ = 13.2 were set.

After applying noise filtering, outliers were detected and removed. These are data points that deviate significantly from the expected range and can distort model training if left unaddressed. Outliers are typically caused by sensor malfunctions, transient states, or rare environmental events that do not reflect the machine's true behavior. The Interquartile Range (IQR) method was used to detect outliers. This method identifies the range within which most data points lie by calculating the interquartile range as the difference between the first (Q1) and third quartiles (Q3). Data points falling below Q1 − 1.5 · IQR or above Q3 + 1.5 · IQR were considered outliers and removed. This method proves to be robust against skewed data distribution and effective for detecting extreme outliers.

This model should be trained to ensure that the dataset corresponds to steady-state operation. To ensure that only steady-state data are used for training the model, a simple yet effective method for identifying transients is to monitor the slope of the signals over time. By calculating the rate-of-change in key variables, such as P and Q, transients were detected when the slope exceeded a predefined threshold.

In short, by applying Gaussian filtering, outlier detection using IQR, and transient data removal based on slope analysis, the dataset was effectively preprocessed for fault classification. Later, a one-hot encoded type of data labeling was used, which consisted of firstly creating a vector of length equal to the number of classes (C = 4) and, secondly, assigning 1 to the position corresponding to the class to which the data belong and 0 to the others. The H-class data after processing are detailed in Table 3, while the data corresponding to each faulty class are detailed in Table 4. The graphical representation of the measurements for each type of state (H, OD, SD, and OP) is provided in Figure 9 in terms of the machine operating conditions [P, Q, U]. The differences among classes were verified in previous studies [8].

Table 3. Experimental tests for class H.

Test Series	Instances	P_{min} [W]	P_{max} [W]	Q_{min} [VAr]	Q_{max} [VAr]	U_{min} [V]	U_{max} [V]	$I_{e,min}$ [mA]	$I_{e,max}$ [mA]
1	1,400,543	41	3352	−1955	2921	371.87	388.81	4.06	532.76
2	1,292,698	−119	3269	−1955	3043	360.36	377.76	3.71	515.43
3	1,310,937	70	3326	−1955	2952	368.01	381.89	3.19	519.05
4	1,249,949	−24	3291	−1955	2893	381.43	394.23	3.56	527.37
5	1,241,603	−102	3213	−1955	2876	384.21	398.73	4.44	535.62
6	1,283,744	−82	3352	−1955	2972	380.29	400.02	3.30	545.92
7	1,384,640	−90	3273	−1955	2993	388.21	397.82	3.07	540.42
8	1,421,319	−165	3211	−1955	2996	402.53	414.17	33.14	550.40
9	1,426,068	−156	3295	−1955	3084	416.05	428.56	69.85	600.41

Table 4. Experimental tests for classes OD, SD, and OP.

Class	Instances	P_{min} [W]	P_{max} [W]	Q_{min} [VAr]	Q_{max} [VAr]	U_{min} [V]	U_{max} [V]	$I_{e,min}$ [mA]	$I_{e,max}$ [mA]
OD	303,714	383	2129	−1665	1130	397.50	404.40	106.91	330.91
SD	90,896	477	2094	−1814	1083	396.66	402.37	102.26	319.02
OP	191,604	458	2311	−1713	1241	394.32	405.86	105.14	339.82

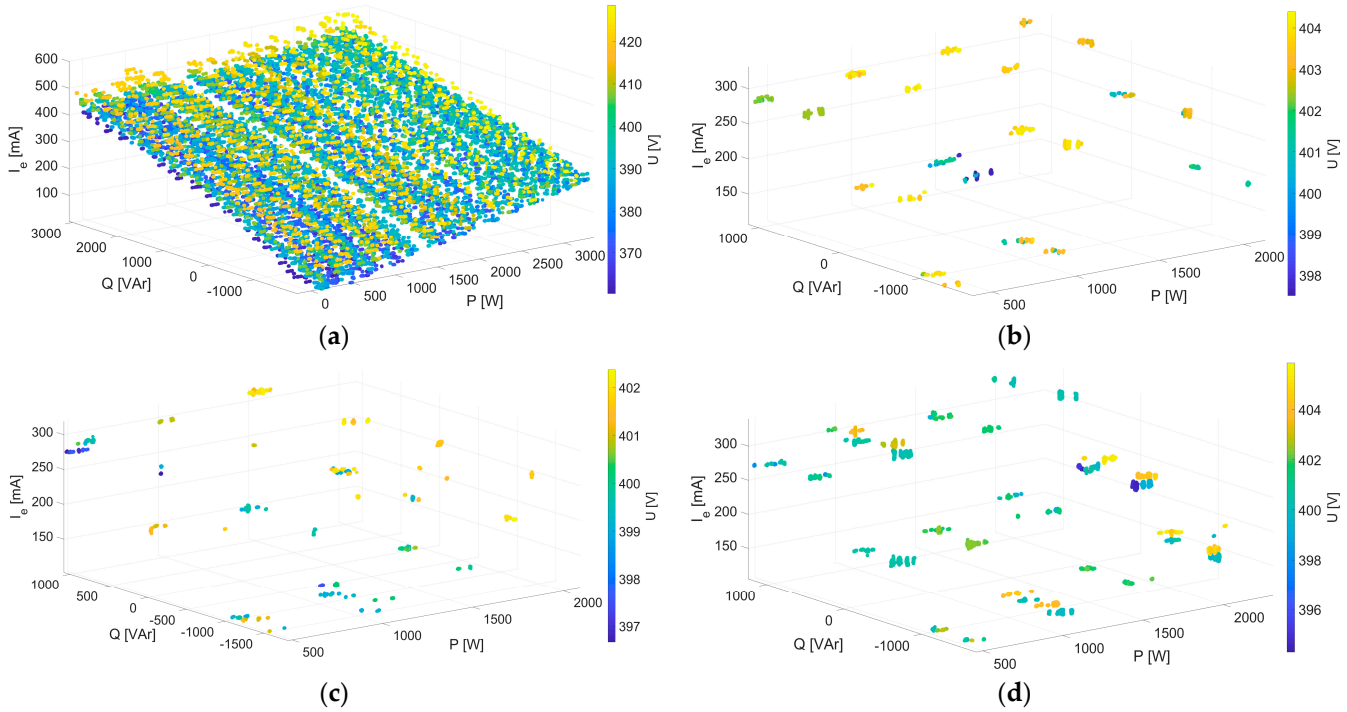

Figure 9. Graphical representation of the measurements after data processing for each class: (**a**) Healthy (H); (**b**) Open-diode (OD); (**c**) Shorted-diode (SD); (**d**) Open-phase (OP).

As shown in Tables 3 and 4, the number of samples of class H is significantly larger compared to the faulty classes. It is important to note that the duration of the faulty condition tests is limited to a few seconds to avoid damaging the excitation system due to overcurrent. This results in a markedly imbalanced dataset dominated by class H data and a narrower [P, Q] range with respect to the class H range so as to limit potential damages to the exciter due to excessive fault currents. Specifically, during the faulty tests, there are up to four times more instances of class H compared to the other classes. When the healthy tests are combined with the faulty tests, there are as many as 1000 instances of class H for every instance of classes OD, SD, or OP, with class SD being the most underrepresented as it implies the most severe conditions for the experimental testbench. For example, a heavily imbalanced dataset hinders the proper training of the model, causing the algorithm to become biased toward the majority class during learning and resulting in a tendency to predict any input as this class. Therefore, it is essential to apply resampling techniques.

To address the class imbalance, the minority classes (OD, SP, OP) were oversampled by generating synthetic samples using SMOTE (Synthetic Minority Oversampling Technique). SMOTE creates new synthetic samples by interpolating between existing samples in the minority classes. On the other hand, the majority class H was undersampled by randomly removing some samples to balance the number of samples across classes in order to prevent this model from becoming biased toward the healthy state.

Finally, to implement effective cross-validation, certain samples were strategically excluded from the training dataset. This step is critical because, given the limited number of independent samples, a naive random split of the data could lead to an overlap of

operational conditions between the training and validation sets. In other words, if the same or very similar operating conditions are present in both sets, the validation data would not provide a reliable measure of the model's ability to generalize, particularly in detecting overfitting. The selection process ensures that all operational conditions are well-represented in both training and validation sets over all the folds, reducing the risk of data leakage. Thus, stratified sampling or controlled randomization was applied in this case, adhering to a distribution ratio of approximately 70% of the samples for training and 30% for validation over four different folds (k = 1 to k = 4). A simplified representation of the k-fold cross-validation carried out is provided in Figure 10.

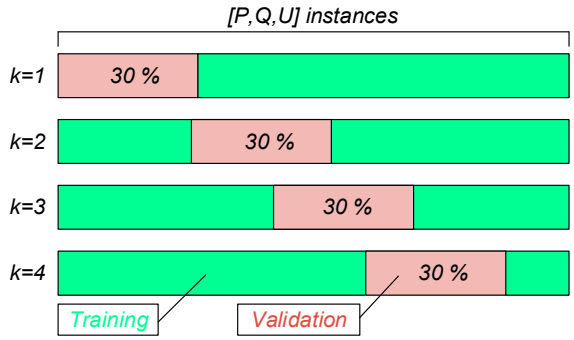

Figure 10. Simplified schema of the k-fold cross-validation.

5.3. Use Case and Implementation

The computational implementation of the proposed model relied on the use of several libraries, with primary emphasis on Torch®, Scikit-learn®, NumPy®, and Pandas®. The Torch library was essential for building and training the neural network models, providing flexibility and efficiency throughout the process. Additionally, Scikit-learn was employed for model evaluation and validation. NumPy and Pandas were used for data manipulation and processing, enabling efficient handling of large and complex datasets. These libraries collectively facilitated the seamless integration of data management, model development, and performance assessment.

The selection of hyperparameters involved an extensive evaluation of model complexity and regularization to prevent overfitting. In the following, a detailed description of the selected hyperparameters is provided:

- Input neurons: The number of input neurons was determined by the four input features (P, Q, U, and I_e);
- Output neurons: The number of output neurons corresponds to the four classes (H, OD, SD, and OP);
- Hidden layers: This model was reduced to two hidden layers after observing that increasing the number of layers resulted in overfitting;
- Neurons per layer: After testing, 15 neurons per hidden layer were chosen, as they provided the best balance between testing and validation accuracy. This configuration allowed the network to capture the essential patterns within each fault type while avoiding overfitting, effectively balancing model complexity with classification accuracy;
- Activation function (f): Four activation functions were tested: Rectified Linear Unit (ReLU); Sigmoid; Hyperbolic Tangent (Tanh); and Scaled Exponential Linear Unit (SeLU). The SeLU function was chosen as it showed the best performance when combined with regularization techniques, improving both training and validation accuracy. This activation function is defined according to Equations (33) and (34):

$$f(x) = SeLU(x) = \lambda \cdot x \;\; if \; x > 0 \tag{33}$$

$$f(x) = SeLU(x) = \lambda \cdot \alpha \cdot (e^x - 1) \;\; if \; x \leq 0 \tag{34}$$

In Equations (33) and (34), $\lambda \approx 1.0507$ and $\alpha \approx 1.6733$ are constants that ensure proper scaling of the outputs for maintaining self-normalization. The key advantage of SeLU over other activation functions is its ability to prevent activations from dying out or exploding over deep layers, enabling better stability in training deep networks. The derivative of SeLU ensures smooth gradient flow during backpropagation, especially for negative inputs, where other functions like ReLU would zero out gradients;

- Optimizer: The Root Mean Square Propagation (RMSProp) optimizer from the Torch library was selected for its superior performance over the Stochastic Gradient Descent (SGD) and the Adaptive Moment Estimation (ADAM) optimizers for this specific application. The RMSProp optimizer is a gradient-based optimization algorithm that adapts the learning rate for each parameter dynamically. The optimizer maintains a moving average of the squared gradients to normalize the updates. This reduces the learning rate for parameters that have been updated frequently, preventing oscillations, and allows for more frequent updates for parameters with less variability. The update rule for RMSProp is expressed in Equation (35):

$$\underline{v}_t = \beta \cdot \underline{v}_{t-1} + (1-\beta) \cdot (\nabla L)^2 \tag{35}$$

In Equation (35), $\underline{v}_t$ and $\underline{v}_{t-1}$ are the moving average of squared gradients at time step t and the previous step $(t-1)$, respectively; β is the decay rate, and ∇L represents the gradient of the loss function with respect to the parameters at step t in the matrix form. The actual parameter update is then performed according to Equation (36):

$$\underline{\theta}_{t+1} = \underline{\theta}_t - \frac{r}{\sqrt{\underline{v}_t + \varepsilon}} \cdot \nabla L \tag{36}$$

In Equation (36), $\underline{\theta}_t$ and $\underline{\theta}_{t+1}$ represent the model's parameters at steps t and t + 1, respectively; r is the learning rate, and ε corresponds to a small constant ($\varepsilon = 10^{-8}$ in this case) to prevent division by zero;

- Learning rate: Set to r = 0.001, initialized to control the rate of parameter updates and prevent this model from being stuck in local minima;
- L1 regularization: A penalty proportional to the absolute value of the weights was applied to reduce model complexity, with a regularization factor of $\alpha_1 = 0.01$;
- L2 regularization: A penalty proportional to the square of the weights was applied, with a regularization factor of $\alpha_2 = 0.1$;
- Dropout: A dropout probability of $p = 0.2$ was applied to prevent overfitting, where during training, a random set of neurons is dropped from the network to ensure generalization.

The final model configuration is summarized in Table 5.

Table 5. Summary of model hyperparameters.

Number of input neurons	4
Number of output neurons	4
Number of hidden layers	2
Neurons per hidden layer	15
Activation function	SeLU
Optimizer	RMSProp
Learning rate (r)	0.001
L1 regularization factor (α_1)	0.01
L2 regularization factor (α_2)	0.10
Dropout probability (p)	0.2

6. Results and Discussion

This section presents the results from the developed automatic fault classification system for rotating rectifier faults in BSMs. The classification task involves distinguishing

between four classes (H, OD, SD, and OP). The model's performance is assessed using a comprehensive set of metrics, including accuracy, precision, recall, F1-score, and confusion matrices. The assessment is carried out both on a healthy/faulty binary distinction basis and on a per-class basis.

For this assessment, the following terms are defined:

- True positives (TP): Instances that are correctly classified as faulty when a fault is actually present;
- False positives (FP): Instances that are incorrectly classified as faulty when no fault is present;
- True negatives (TN): Instances that are correctly classified as healthy when no fault is present;
- False negatives (FN): Instances that are incorrectly classified as healthy when a fault is actually present.

These definitions apply consistently across each fault classification task, where each fault type (OD, SD, OP) and the healthy state (H) are considered separate classes.

6.1. Accuracy

The accuracy measures the proportion of correct classifications (TP and TN) relative to all classifications (TP, FP, TN, and FN), according to Equation (37).

$$Accuracy = \frac{TP + TN}{TP + TN + FP + FN} \tag{37}$$

This model achieved an overall classification accuracy of 93.4% when distinguishing between healthy and faulty states. On the other hand, the overall accuracy for classifying each individual case (H, OD, SD, and OP) was 84.9%. This accuracy is lower than the overall accuracy for distinguishing healthy/faulty states, reflecting the challenge of correctly identifying the specific fault once a class different from H is detected.

6.2. Precision

The precision indicates the proportion of correct positive predictions (i.e., when this model predicts a specific fault, how often it is correct), according to Equation (38). High precision ensures that FP is minimized.

$$Precision = \frac{TP}{TP + FP} \tag{38}$$

This model showed very high precision for detecting the H class, achieving 92%. This high precision is a positive aspect of this model as it minimizes the false alarms, indicating faults under healthy conditions. The precision for detecting that a fault is present, without yet distinguishing its type, was 94.9%. This low false positive rate for faults ensures that this model does not often mistake a healthy state with a faulty one, which is crucial for ensuring reliability. In the per-class analysis, for the OD class, the precision was relatively low at 83.3%, indicating that approximately the fifth part of the predictions of OD faults were confused or misclassified. The precision for SD and OP faults were slightly better, reaching 86.2% and 88.1%, respectively. These results show that this model is highly effective at minimizing false signals, although it underperforms when identifying OD faults.

6.3. Recall

The recall measures the model's ability to identify all actual positives (i.e., faults), ensuring that FN is minimized. This metric is particularly important in fault detection applications. The recall metric is calculated as per Equation (39).

$$Recall = \frac{TP}{TP + FN} \tag{39}$$

This model correctly identified 95% of all actual healthy states. This high recall for the healthy state shows that this model rarely misclassifies a healthy machine as faulty. Recall for fault detection was slightly lower at 91.8%, meaning that around 8.2% of actual faults were misclassified as healthy states, which represents a relatively high value. In the per-class analysis, the recalls for OD, SD, and OP were 76.9%, 85.7%, and 82%, respectively. This indicates that, while this model performs well, OD is the least sensitive class, i.e., the most prone to misclassification.

6.4. F1-Score

The F1-score is the harmonic mean of precision and recall, balancing both metrics to provide a single measure of performance, following Equation (40).

$$F1 = 2 \cdot \frac{Precision \cdot Recall}{Precision + Recall} \tag{40}$$

The F1-score was 93.5% for the H class, representing a balanced performance between precision and recall. On the other hand, the F1-score for detecting that a fault was present was 93.3%, also indicating a fair balance. In the per-class analysis, the F1-score for OD, SD, and OP were 80%, 85.9%, and 84.9%, respectively. This balance reflects a fair performance in fault detection for SD and OP, while for OD, there is room for balance improvement.

The class-specific metrics (precision, recall, and F1-Score) are presented in Figure 11; both the healthy/faulty binary distinction approaches, in Figure 11a; and the per-class approach, in Figure 11b. The healthy class's higher recall but lower precision reflects the model's sensitivity to correctly capturing healthy states while occasionally misinterpreting subtle fault conditions as healthy.

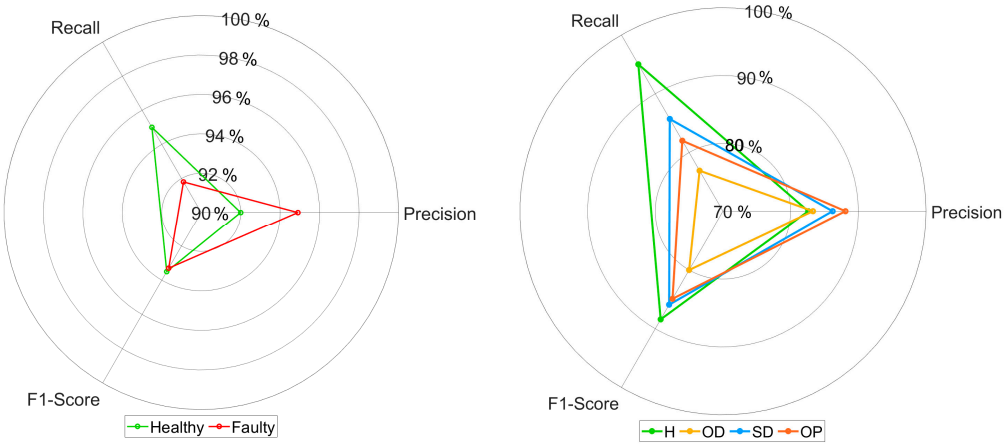

Figure 11. Class-specific metrics: (**a**) Binary simplified analysis; (**b**) Full per-class analysis.

6.5. Confusion Matrices

The confusion matrix provides a detailed breakdown of model predictions, showing TP, TN, FP, and FN for each class. This matrix helps visualize where this model outperforms and where it commits larger classification errors. Table 6 shows the binary confusion matrix, distinguishing between healthy and faulty states, while Table 7 provides the full confusion matrix across all operational states (H, OD, SD, and OP). The full confusion matrix highlights that the majority of errors occur between similar fault types, such as OD and OP, which can have overlapping features under certain machine conditions. The results for the full confusion matrix are depicted in Figure 12 for each class.

Table 6. Confusion matrix: binary simplified.

	Healthy Predicted	Faulty Predicted
Healthy Actual	95.0%	5.0%
Faulty Actual	8.2%	91.8%

Table 7. Full confusion matrix.

	H Predicted	OD Predicted	SD Predicted	OP Predicted
Actual H	95.0%	2.0%	1.5%	1.5%
Actual OD	7.6%	76.9%	8.7%	6.8%
Actual SD	5.4%	6.1%	85.7%	2.8%
Actual OP	7.1%	7.3%	3.6%	82.0%

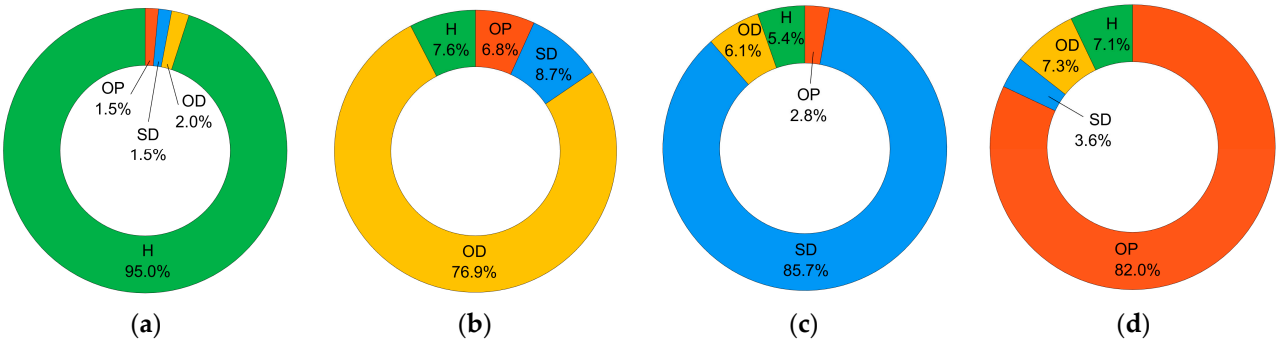

Figure 12. Graphical representation of the measurements after data processing for each class: (**a**) Healthy (H); (**b**) Open-diode (OD); (**c**) Shorted-diode (SD); (**d**) Open-phase (OP).

6.6. Discussion

The experimental results confirm that this model performs reasonably well in detecting and classifying the operational states of the rotating rectifier in BSMs. A key strength of the obtained results lies in the model's ability to maintain high precision and recall for most fault types, particularly SD and OP, despite challenging operational environments. The neural network's architecture, with its multiple layers and advanced regularization techniques, contributes significantly to its robustness. The model's strong performance can be attributed to several factors, including data processing, the use of SMOTE for balancing, and the advanced neural network design based on MLP architecture coupled with dropout regularization and RMSProp optimization. The experimental setup, which included a modified BSM allowing direct access to the rectifier, provided a comprehensive dataset for model training. The fault-specific patterns captured during the tests were integral to the network's success in real-time classification.

The results validate the proposed automatic fault detection method's effectiveness for BSMs. This model achieves state-of-the-art performance, particularly in detecting and classifying SD and OP faults, making it a valuable tool for real-time condition monitoring in industrial applications. This approach not only improves accuracy but also addresses the computational challenges of online fault detection, positioning it as a leading solution for rotating rectifier fault classification in BSMs.

However, certain limitations of this work should also be addressed, particularly regarding the OD class. The OD fault is inherently the least severe among rotating rectifier fault types, posing a challenge for the classifier in distinguishing it from the H state. Unlike SD and OP faults, OD faults do not significantly disrupt machine performance and often manifest as minor deviations in excitation current or reactive power, which may be interpreted as normal fluctuations. An open diode primarily causes a subtle reduction in rectified DC output voltage, rather than the drastic DC voltage drops seen in SD faults—followed by excitation current spikes or reactive power aggressive drops—or the

severe phase imbalances characteristic of OP faults. Consequently, the classifier struggles to distinguish between the OD and H states, leading to occasional misclassifications.

Furthermore, SD faults are analogous to phase-to-phase solid faults. To avoid potential damage to the exciter during experimental testing, these short circuits were not fully solid. Instead, a limiting resistor was used to reduce fault currents, necessary to prevent currents reaching 10–15 per unit that could damage the exciter windings and the rest of the excitation circuit. The use of a limiting resistor, however, reduces the observable difference between SD and other faults. Under a true solid short-circuit scenario, SD faults would exhibit larger differences with the other classes. This limitation suggests that in practical, unmitigated conditions, the classifier would likely distinguish SD faults from other faults more effectively.

Additionally, the current demand for excitation at a given operating point has been shown to depend on the resistance of the excitation circuit, which varies with temperature [37]. However, in the present experimental setup, temperature control was not applied, resulting in unmonitored thermal variations that may affect the excitation current in ways resembling OD faults. As temperature rises, excitation winding resistance increases, necessitating a higher excitation current to maintain the desired output. These temperature-induced changes can mimic the excitation current or reactive power shifts seen in OD faults, potentially causing the classifier to misinterpret these temperature variations as fault-related. Future tests could address heating effects as an additional variable to better isolate true OD faults from temperature-induced fluctuations.

In summary, limitations in OD fault classification stem from the inherently subtle impact of OD faults on power electronics behavior, overlapping characteristics with the H state—including temperature-induced variations—and experimental constraints that limit the manifestation of high fault currents.

7. Conclusions

This research introduces an advanced automatic classification method for rotating rectifier faults in brushless synchronous machines (BSMs). The developed approach leverages a multilayer perceptron (MLP) neural network to classify the machine's operational states, including healthy conditions and the most common fault types: open-diode (OD); shorted-diode (SD); and open-phase (OP). By employing key machine measurements ordinarily available in industrial applications, such as active power (P), reactive power (Q), stator voltage (U), and excitation current (I_e), the proposed method offers a non-invasive real-time fault classification solution, with low computational complexity and without the need for specialized diagnostic relays or sensors.

The key findings of this study can be summarized as follows:

1. High Accuracy and Robustness: The neural network achieved a classification accuracy of 93.4% across all operational states and 84.9% when distinguishing between individual faults. This high performance reflects the model's robustness in real-world scenarios, supported by the use of advanced regularization techniques and careful tuning of hyperparameters;
2. Strong Performance on Specific Faults: This model excelled in detecting SD and OP faults, with precision and recall scores of at least 86.2% and 82%, respectively. These results highlight the model's ability to accurately identify critical faults. The accuracy in detecting OD faults, while slightly lower metrics (83.3% precision and 76.9% recall), remains satisfactory for industrial applications;
3. Effective Preprocessing and Data Balancing: The preprocessing techniques applied, including Gaussian filtering for noise reduction, outlier detection, and class balancing using SMOTE, were critical to improving the dataset quality and ensuring reliable model performance. These steps helped mitigate the impact of imbalanced data, a common issue in industrial settings where healthy states dominated the dataset;
4. Real-Time Applicability: The proposed method is highly suited for real-time applications, as it classifies machine states quickly and efficiently. This non-invasive approach

allows for continuous monitoring without the need for manual inspections or downtime, significantly improving machine reliability and reducing maintenance costs;

5. Experimental Validation: The network was trained, and the model's performance was validated based on rigorous experimental testing on a modified BSM setup, which allowed access to the rotating rectifier. The induced faults and controlled operational conditions provided a reliable dataset, contributing to the accuracy of the classification results.

Despite its promising results, this study also identified some limitations, particularly in the classification of OD faults, where overlapping features with other fault types affected the model's performance to a larger extent. Future research should focus on enhancing the detection of OD faults by incorporating more advanced neural network architectures, such as recurrent neural networks (RNNs) or long short-term memory (LSTM) networks, which are well-suited for time-series data and can better capture transient behaviors. Additionally, the application of transfer learning techniques should be explored to enable the model's adaptation to different machine types or operating environments. Furthermore, additional online non-electrical measurable variables, such as temperature, could be considered as inputs to better isolate true OD faults from temperature-induced fluctuations.

To extend the model's robustness across the full operational space, future work shall involve developing a synthetic dataset that expands the fault scenarios over a broader range of active and reactive power levels, as well as to solid SD faults. Integrating these synthetic data with the experimental data enables the model's generalization capacity and ensures accurate fault classification in previously untested operating regions. This approach is especially beneficial for larger machines, where generating real fault data are impractical, thus supporting scalable model training across machines of varying sizes and power ratings.

In fact, the requirement for a substantial dataset of faulty machine conditions to effectively train the neural network is considered the main limitation of the proposed approach. Rotating rectifier faults, particularly shorted-diode faults, generate severe overcurrents that can result in significant damage if not cleared promptly. Consequently, conducting experimental tests on large machines under faulty conditions is impractical due to the associated risks and costs. This dependency on extensive fault data contrasts with other techniques, such as exciter field current ripple or flux monitoring methods, which operate without the need for a data pool or a learning phase.

To mitigate this limitation, alternative approaches can be explored. Experimental tests conducted at reduced power levels may provide a safer scenario, with potential compromises in representativeness for full-power machine operation. Additionally, synthetic data generation and advanced simulations offer promising avenues to expand the training dataset. These methods can replicate faulty conditions under controlled scenarios, enabling the neural network to learn fault characteristics without exposing machines to real faults. However, the accuracy of such approaches is inherently dependent on the fidelity of the models and assumptions used during data generation, which remains a critical area for further investigation.

In conclusion, this study presents a reliable, real-time fault classification system for rotating rectifiers in BSMs. The combination of neural network-based classification, robust preprocessing techniques, and experimental validation provides a solid foundation for future advancements in automatic fault detection systems for industrial machinery. The proposed system offers a significant step forward in improving machine reliability, minimizing downtime, and optimizing maintenance practices.

Author Contributions: Conceptualization, K.M. and C.A.P.; methodology, K.M. and J.D.; software, J.D.; validation, K.M., R.P., J.M.G. and C.A.P.; formal analysis, K.M., R.P., J.M.G. and C.A.P.; investigation, K.M. and R.P.; resources, C.A.P.; data curation, K.M.; writing—original draft preparation, K.M. and J.D.; writing—review and editing, K.M., R.P., J.M.G. and C.A.P.; visualization, K.M.; supervision, C.A.P.; project administration, K.M.; funding acquisition, C.A.P. All authors have read and agreed to the published version of the manuscript.

Funding: This research received no external funding.

Data Availability Statement: The original contributions presented in this study are included in this article. Further inquiries can be directed to the corresponding author.

Acknowledgments: The authors acknowledge the contribution of Sofía Lobera and Carlos González-Guillén to the initial stage of this work, within the scope of the Master's Thesis of Sofía Lobera supervised by Kumar Mahtani and Carlos González-Guillén.

Conflicts of Interest: The authors declare no conflicts of interest.

References

1. Nøland, J.K.; Nuzzo, S.; Tessarolo, A.; Alves, E.F. Excitation System Technologies for Wound-Field Synchronous Machines: Survey of Solutions and Evolving Trends. *IEEE Access* **2019**, *7*, 109699–109718. [CrossRef]
2. Kang, J.-B.; Lee, J.-Y.; Nguyen, T.; Kim, H.-J.; Lee, J.-H. Effects of Material Deformation Due to Aging of Electrical Steel on the Brushless Wound-Field Synchronous Generator. *Electronics* **2023**, *12*, 2279. [CrossRef]
3. *IEEE Std C37 102-2006 (Revision of IEEE Std C37 102-1995)*; IEEE Guide for AC Generator Protection. IEEE: New York, NY, USA, 2006; pp. 1–177.
4. *IEEE Std C50.13-2014 (Revision of IEEE Std C50.13-2005)*; IEEE Standard for Cylindrical-Rotor 50 Hz and 60 Hz Synchronous Generators Rated 10 MVA and Above. IEEE: New York, NY, USA, 2014; pp. 1–63.
5. *IEEE Std C50.12-2005*; IEEE Standard for Salient-Pole 50 Hz and 60 Hz Synchronous Generators and Generator/Motors for Hydraulic Turbine Applications Rated 5 MVA and Above. IEEE: New York, NY, USA, 2006; pp. 1–45.
6. Dulas, J.H.; Chisholm, M.; Griffith, T.; Ocmand, J. API 546, 4th Edition—Making It Easier to Specify Brushless Synchronous Machines. In Proceedings of the 2019 IEEE Petroleum and Chemical Industry Committee Conference (PCIC), Vancouver, BC, Canada, 9–12 September 2019; pp. 41–50.
7. Pallantla, M.; Kumar, P.; Mohan, N. Comparison and Evaluation of the Different Brushless Excitation Topologies for Synchronous Machines-A Literature Survey. In Proceedings of the 2020 IEEE International Conference on Power Electronics, Smart Grid and Renewable Energy (PESGRE2020), Cochin, India, 2–4 January 2020; pp. 1–6.
8. Mahtani, K.; Guerrero, J.M.; Beites, L.F.; Platero, C.A. Application of a Model-Based Method to the Online Detection of Rotating Rectifier Faults in Brushless Synchronous Machines. *Machines* **2023**, *11*, 223. [CrossRef]
9. Batzel, T.D.; Swanson, D.C.; Defenbaugh, J.F. Predictive diagnostics for the main field winding and rotating rectifier assembly in the brushless synchronous generator. In Proceedings of the 4th IEEE International Symposium on Diagnostics for Electric Machines, Power Electronics and Drives (SDEMPED), Atlanta, GA, USA, 24–26 August 2003; pp. 349–354.
10. Cai, Y.; Hao, L.; Chen, J.; Duan, X.; Xiong, G.; He, P.; Wang, N.; Wang, G. Analysis and Monitoring of the Fuse Conditions in Nuclear Power Multiphase Brushless Excitation System. *IEEE Trans. Ind. Inform.* **2024**, *20*, 8559–8571. [CrossRef]
11. Kim, H.J.; Shaikh, M.F.; Lee, S.B.; Platero, C.A.; Kim, T. Alternative Test Methods for Monitoring the Condition of Brushless Exciters in Synchronous Machines. *IEEE Trans. Energy Convers.* **2022**, *37*, 2009–2018. [CrossRef]
12. Li, X.; Liu, W.; Jiao, N.; Sun, C.; Mao, S. Fault Diagnosis of Rotating Rectifier in Aircraft Wound-Rotor Synchronous Starter–Generator Based on Stator Currents Under all Operational Processes. *IEEE Trans. Power Electron.* **2023**, *38*, 16072–16084. [CrossRef]
13. Sun, C.; Liu, W.; Han, X.; Zhang, X.; Jiao, N.; Mao, S.; Wang, R.; Guan, Y. High-Frequency Voltage Injection-Based Fault Detection of a Rotating Rectifier for a Wound-Rotor Synchronous Starter/Generator in the Stationary State. *IEEE Trans. Power Electron.* **2021**, *36*, 13423–13433. [CrossRef]
14. Salah, M.; Bacha, K.; Chaari, A. Detection of Brushless Exciter Rotating Diodes Failures by Spectral Analysis of Main Output Voltage. In Proceedings of the 2013 International Conference on Electrical Engineering and Software Applications, Hammamet, Tunisia, 21–23 March 2013; pp. 1–6.
15. Rahnama, M.; Vahedi, A.; Alikhani, A.M.; Takorabet, N. Diode Open-Circuit Fault Detection in Rectifier Bridge of the Brushless Synchronous Generator. In Proceedings of the 2018 XIII International Conference on Electrical Machines (ICEM), Alexandroupoli, Greece, 3–6 September 2018; pp. 1821–1826.
16. Pang, J.; Liu, W.; Wei, Z.; Sun, C.; Jiao, N.; Han, X. Online Diode Fault Detection in Rotating Rectifier of the Brushless Synchronous Starter Generator. *IEEE Trans. Ind. Inform.* **2020**, *16*, 6943–6951. [CrossRef]
17. Rahnama, M.; Vahedi, A. Rotary Diode Failure Detection in Brushless Exciter System of Power Plant Synchronous Generator. In Proceedings of the 2016 6th Conference on Thermal Power Plants (CTPP), Tehran, Iran, 19–20 January 2016; pp. 6–11.
18. Zhu, P.; Liu, Y.; Fan, B. Fault Diagnosis of the Rotating Rectifier Diode Over a TSSM Based on the Armature Current Calculation and Similarity Measurement. *IEEE Access* **2022**, *10*, 48031–48038. [CrossRef]
19. McArdle, M.G.; Morrow, D.J. Noninvasive Detection of Brushless Exciter Rotating Diode Failure. *IEEE Trans. Energy Convers.* **2004**, *19*, 378–383. [CrossRef]
20. Sottile, J.; Trutt, F.C.; Leedy, A.W. Condition Monitoring of Brushless Three-phase Synchronous Generators with Stator Winding or Rotor Circuit Deterioration. *IEEE Trans. Ind. Appl.* **2006**, *42*, 1209–1215. [CrossRef]

21. Cui, J.; Tang, J.; Shi, G.; Zhang, Z. Generator Rotating Rectifier Fault Detection Method Based on Stacked Auto-encoder. In Proceedings of the 2017 IEEE Workshop on Electrical Machines Design, Control and Diagnosis (WEMDCD), Nottingham, UK, 20–21 April 2017; pp. 256–261.
22. Ahmadi, A.; Mahbubi, S.; Shahnazari, M. Rotating Rectifier Fault Detection in Brushless Excitation System of Synchronous Generators. In Proceedings of the 2019 27th Iranian Conference on Electrical Engineering (ICEE), Yazd, Iran, 30 April–2 May 2019; pp. 1–5.
23. Zhang, C.; Xia, L. A Novel Online Diagnosis of Brushless Generator Rotary Rectifier Fault. In Proceedings of the 2008 International Conference on Electrical Machines and Systems, Wuhan, China, 17–20 October 2008; pp. 835–838.
24. Cai, Y.; Hao, L.; Zhou, Y.; Chen, J.; Hu, Q.; Duan, X.; Wang, G. Rotating Rectifier Fault Diagnosis of Nuclear Multiphase Brushless Excitation System Based on DTW Metric and kNN Classifier. *IEEE Trans. Power Electron.* **2023**, *38*, 10329–10343. [CrossRef]
25. Chen, J.; Hao, L.; Li, H.; Zhang, L. Time–Frequency Characteristics Analysis and Diagnosis of Rotating Rectifier Faults in Multiphase Annular Brushless System. *IEEE Trans. Ind. Electron.* **2023**, *70*, 3233–3244. [CrossRef]
26. Rahnama, M.; Vahedi, A.; Alikhani, A.M.; Montazeri, A. Machine-learning Approach for Fault Detection in Brushless Synchronous Generator Using Vibration Signals. *IET Sci. Meas. Technol.* **2019**, *13*, 852–861. [CrossRef]
27. Rahnama, M.; Vahedi, A. Application of Acoustic Signals for Rectifier Fault Detection in Brushless Synchronous Generator. *Arch. Acoust.* **2019**, *44*, 267–276.
28. Mohammad-Alikhani, A.; Rahnama, M.; Vahedi, A. Neighbors Class Solidarity Feature Selection for Fault Diagnosis of Brushless Generator Using Thermal Imaging. *IEEE Trans. Instrum. Meas.* **2020**, *69*, 6221–6227. [CrossRef]
29. Tian, P.; Guerrero, J.M.; Platero, C.A.; Lee, S.B.; Gyftakis, K.N.; Antonino-Daviu, J. Condition Monitoring of Rotating Diodes in Synchronous Machines Through the Exciter Stray Flux Analysis. *IEEE Trans. Ind. Appl.* **2023**, *59*, 3175–3185. [CrossRef]
30. Salah, M.; Bacha, K.; Chaari, A.; Benbouzid, M.E.H. Brushless Three-Phase Synchronous Generator Under Rotating Diode Failure Conditions. *IEEE Trans. Energy Convers.* **2014**, *29*, 594–601. [CrossRef]
31. Li, X. A Microprocessor-based Fault Monitor for Rotating Rectifiers of Brushless AC Exciters Using a Pattern-Recognition Approach. In *Advanced Technologies in I & M, Proceedings of the 10th Anniversary IMTC/94—1994 IEEE Instrumentation and Measurement Technology Conference, Hamamatsu, Japan, 10–12 May 1994*; Institute of Electrical and Electronics Engineers: Piscataway, NJ, USA, 1994; pp. 394–397.
32. Wu, Y.; Cai, B.; Ma, Q. An Online Diagnostic Method for Rotary Diode Open-Circuit Faults in Brushless Exciters. *IEEE Trans. Energy Convers.* **2018**, *33*, 1677–1685. [CrossRef]
33. Zouaghi, T.; Poloujadoff, M. Modeling of Polyphase Brushless Exciter Behavior for Failing Diode Operation. *IEEE Trans. Energy Convers.* **1998**, *13*, 214–220. [CrossRef]
34. Bui, H.K.; Bracikowski, N.; Hecquet, M.; Zappellini, K.L.; Ducreux, J.P. Simulation of a Large Power Brushless Synchronous Generator (BLSG) with a Rotating Rectifier by a Reluctance Network for Fault Analysis and Diagnosis. *IEEE Trans. Ind. Appl.* **2017**, *53*, 4327–4337. [CrossRef]
35. Tantawy, A.; Koutsoukos, X.; Biswas, G. Aircraft Power Generators: Hybrid Modeling and Simulation for Fault Detection. *IEEE Trans. Aerosp. Electron. Syst.* **2012**, *48*, 552–571. [CrossRef]
36. Rahnama, M.; Vahedi, A.; Alikhani, A.M.; Nobahari, A. Numerical Modeling of Brushless Synchronous Generator for Rectifier Fault Detection. In Proceedings of the 2019 19th International Symposium on Electromagnetic Fields in Mechatronics, Electrical and Electronic Engineering (ISEF), Nancy, France, 29–31 August 2019; pp. 1–2.
37. Pascual, R.; Rivero, E.; Guerrero, J.M.; Mahtani, K.; Platero, C.A. Influence of Temperature on Brushless Synchronous Machine Field Winding Interturn Fault Severity Estimation. *Appl. Sci.* **2024**, *14*, 8061. [CrossRef]